Corrosion Communications 6 (2022) 16–28

Contents lists available at ScienceDirect

Corrosion Communications

journal homepage: www.elsevier.com/locate/corcom

Research article

In vitro degradation and biocompatibility of vitamin C loaded Ca-P coating on a magnesium alloy for bioimplant applications

Xue-Mei Wang [a], Guan-Jie Lu [a], Lan-Yue Cui [a], Cheng-Bao Liu [a], M. Bobby Kannan [b,c], Fen Zhang [a], Shuo-Qi Li [a], Yu-Hong Zou [d], Rong-Chang Zeng [a,*]

[a] Corrosion Laboratory for Light Metals, College of Materials Science and Engineering, Shandong University of Science and Technology, Qingdao 266590, China
[b] School of Engineering, University of Newcastle, Callaghan, New South Wales 2308, Australia
[c] College of Science and Engineering, James Cook University, Townsville, Queensland 4811, Australia
[d] School of Chemical and Biological Engineering, Shandong University of Science and Technology, Qingdao 266590, China

ARTICLE INFO

Article history:
Received 4 January 2022
Received in revised form 17 March 2022
Accepted 17 March 2022
Available online 12 May 2022

Keywords:
Magnesium alloy
Ca-P coating
Degradation
Vitamin C
Biomaterial

ABSTRACT

Molecular recognition was utilized to fabricate bioinspired calcium phosphate (Ca-P) coating on bioabsorbable magnesium alloys through small biomolecules such as Vitamin C (VC). Ca-P and VC hybrid coating (Ca-P_{VC}) was successfully fabricated on AZ31 Mg alloy. The surface morphology and chemical composition of the coatings were investigated using SEM, XRD, and FTIR together with XPS. The results showed that the Ca-P_{VC} coating was composed of bamboo leaf-like Ca-P particles with a thickness of about three times that of the Ca-P coating. The surface roughness of the Ca-P_{VC} coating (1.12 ± 0.12 μm) was lower than that (3.14 ± 1.93 μm) of Ca-P coating, suggesting the formation of refined Ca-P particles resulting from the VC addition. The corrosion resistance of the coated samples was characterized via electrochemical polarization, impedance spectroscopy, and immersion hydrogen evolution tests. The cell toxicity of the coated samples was evaluated utilizing mouse MC3T3-E1 pre-osteoblasts. The charge transfer resistance (R_{ct}) of the Ca-P_{VC} coated alloy increased as compared to the bare and Ca-P coated alloy samples. The Ca-P_{VC} coated alloy exhibited minimal corrosion current density (1.36×10^{-6} A cm^{-2}), which is one order of magnitude lower in comparison to that of the Ca-P coated alloy. These results confirm that VC addition greatly enhanced the coating resistance on AZ31 Mg alloy. It was also noticed that the Ca-P_{VC} coated samples rapidly induced the formation of apatite after immersion in Hank's solution. VC was mainly transformed to L-Threonic acid, which facilitated the nucleation process of the Ca-P_{VC} coating and significantly increased the thickness, density, and bonding strength of the coating. With enhanced corrosion resistance property and excellent biocompatibility, Ca-P_{VC} coating has great potential for application in biodegradable Mg-based alloys.

1. Introduction

Typically, the fracture of the bone is prone to occur due to various types of traumas or natural aging. In the case of severe bone fracture, the repair is usually performed via the use of non-degradable or inert metal implants such as Ti alloys. However, there are serious challenges, e.g. stress shielding effect, associated with non-degradable metal implants [1,2]. Magnesium (Mg) and its alloys are degradable in the body fluid and hence have the potential to be used as degradable temporary implants, provided that their degradation rate is controlled. There are many reports on calcium phosphate (Ca-P) coating on Mg and its alloys to control their degradation rate [3,4]. An important advantage of Ca-P coating is its high biocompatibility [5,6]; however, mechanical damage to the coating could significantly affect the degradation behavior of the base metal [7–9].

The use of organic additives or inhibitors has been one of the best options available for the protection of Mg and its alloys against degradation [10–12]. Generally, the initial mechanism in any degradation inhibition process is the adsorption of inhibitors on the metal surface. The inhibition of degradation can be a process that involves the for-

* Corresponding author.
E-mail address: rczeng@foxmail.com (R.-C. Zeng).

https://doi.org/10.1016/j.corcom.2022.03.004

mation of chelates on the metal surface, which involves the transfer of electrons from the organic compounds to the surface of Mg and its alloys and thus the formation of a coordinate covalent bond [13]. So far, there is a great deal of research regarding on the use of inhibitors on phosphate conversion coatings to improve the degradation resistance of Mg and its alloys [14,15]. However, the biocompatibility of the phosphate conversion coatings has not been concerned.

The physiological solution in the human body contains both inorganic ions and organic components (e.g. amino acids, proteins, glucose, and vitamins) [16–19]. Once an orthopedic device is implanted in the human body, the interaction occurs between the interfaces of the implanted material and its physiological micro-environment. Wang et al. [20] in our group systematically investigated the degradation mechanism of pure Mg in PBS with alanine, lysine, and glutamic acid, and further explored the influences of isoelectric point, electrical charges, and molecular structure of the representative amino acids on the degradation behavior of pure Mg in PBS. It is demonstrated that the charges of the amino acids make a significant contribution to retarding the degradation of Mg alloy. The effect of proteins and MAO coatings on biodegradable Mg alloys was reported by Zhang et al. [18]. The composite coatings significantly reduce the degradation rate of Mg alloy AZ31 in simulated body fluid (SBF). The formation of $(RCH(NH_2)COO)_2Mg$ by the combination of BSA ($RCH(NH_2)COO$) molecules with Mg^{2+} ions plays an important role in inhibiting the attack of corrosive ions. Yan et al. [17] explored the effect of glucose and albumin on the degradation behavior of pure Mg in physiological saline solution. The synergistic effect of glucose and albumin retards the adsorption of aggressive chloride ions, and thus greatly manipulates the degradation of the pure Mg substrate. Interestingly, glucose promotes the adsorption of albumin on the Mg alloy surface. Nevertheless, the influence of Vitamin C (VC, $C_6H_8O_6$) in the chemical conversion solution for the growth of Ca-P coating on Mg alloy has not been studied in detail.

VC, also known as ascorbic acid, is a water-soluble vitamin found mostly in fruits and vegetables [11]. The optimal intake of VC is 75-90 mg d^{-1} for adults, and possibly higher in certain circumstances. It is an effective anti-inflammatory compound and serves a variety of functions, including wound healing and stimulates the inflammatory response and improves resistance to infection by increasing white blood cell activity. VC also plays an important role in the hydroxylation of the essential amino acids, which are needed in collagen synthesis. It is responsible for the neutralization of radicals in water and acts as a reducing agent by electron donation. VC works as a donor of electrons in all known physiological and biochemical reactions. Moreover, L-Threonic acid (L-TA) is one of the main degradation products of VC in the body metabolism. As a metal ion carrier, L-TA can be easily combined with amino acids or proteins and is further absorbed and utilized by the body. Clinical studies have demonstrated that L-TA has bone resorption of osteoclasts in vitro, and its effect may be related to its radical.

Chidiebere et al. [21] investigated the inhibitive effect of VC on corrosion on mild steels in 1 mol/L HCl and 0.5 mol/L H_2SO_4 environment and observed the chemisorption of VC as the primary mechanism of corrosion inhibition. In addition, quantum chemical calculation results revealed that the oxygen atoms in the VC molecule are the active sites by which the inhibitor molecules can directly adsorb on a mild steel surface. Electrochemical measurements and quantum-chemical calculations of the electron properties of the ZnO nanoparticles/VC hybrid material were performed by Mydlova et al. [22]. It is reported that the degradation rate of the ZnO nanoparticles in Hank's solution decreased when VC was present in the solution. The VC molecules act as a natural inhibitor in the degradation process but its mechanism remains unclear from the degradation perspective. Hence, an in-depth analysis is needed to correlate the molecular structure of VC and its degradation inhibition mechanism. A systematic study on the formation, degradation mechanisms, and biocompatibility of VC-loaded Ca-P coating on AZ31 Mg alloy was carried out in this work.

2. Experimental

2.1. Materials

The substrate material used in this study was AZ31 Mg alloy. The samples with the dimensions of 20 mm × 20 mm × 5 mm were wet-polished using silicon-carbide sandpaper (grade #150 to #2500), degreased in absolute ethanol, and then dried in warm air. All the chemical reagents used for preparing the electrolytes were of analytical grade (Qingdao Jingke Chemical Reagent Co. Ltd., China).

2.2. Coating preparation

The coatings were fabricated on Mg alloy AZ31 substrate in a water bath, as schematically illustrated in Fig. 1. The solution of Ca-P coating was prepared by dissolving $CaCl_2$ (0.25 mol/L) and KH_2PO_4 (0.25 mol/L) in a certain volume of deionized water. For the Ca-P_{VC} coating solution, 0.1 g/L VC was added to the Ca-P coating solution under magnetic stirring at room temperature. Subsequently, the samples were immersed in the Ca-P coating solution and Ca-P_{VC} coating at 60 °C for 30 min in the water bath. Finally, the treated samples were retracted, rinsed with deionized water, and dried with warm air.

2.3. Surface characterization

The surface morphologies and elemental compositions of the samples were characterized using scanning electron microscopy (SEM, Nova Nano SEM 450) equipped with an energy dispersive spectrometer (EDS). The thickness and elemental distribution of the coatings were determined via the cross-section of the samples using SEM. X-ray diffractometer (XRD, Rigaku D/MAX2500PC) analysis, with Cu K_α radiation ($\lambda = 0.154$ nm) in a 2θ scan ranging from 5° to 80° with a scanning rate of 8° min^{-1} was used to determine the different phases of the samples. The functional groups of the coatings were analyzed using Fourier to transform infrared (FT-IR, Nicolet 380) in the wavenumber range from 4000 to 400 cm^{-1} with a resolution of 8 cm^{-1}. The chemical state determination and depth profiling of the coatings were done by means of X-ray photoelectron spectrometer (XPS, ESCALAB250Xi) with monochromatized Al K_α radiation. The surface roughness of coatings was determined by infinite focus microscopy (IFM, Zeta-20).

2.4. Bonding strength

Adhesion measurement was evaluated by ASTM D3359−09 "Standard Test Methods for Measuring Adhesion by Tape Test" on the coated alloy sample. The cross scratch lines were cut on the samples by a tungsten carbide cutting tool. Then the tape was pressed on the surface for 5-10 s and tore off quickly [23].

2.5. Corrosion tests

Electrochemical impedance spectroscopy (EIS) and potentiodynamic polarization (PDP) tests were conducted on an electrochemical workstation (Versa Stat 4) to evaluate the corrosion behavior of the uncoated, Ca-P coating, and Ca-P_{VC} coating in Hank's solution at room temperature.

The electrochemical tests were performed using a standard three-electrode system with platinum as the counter electrode, saturated calomel electrode (SCE) as the reference, and the sample with an exposed area of 1 cm^2 as the working electrode. The open circuit potential (OCP) values were recorded during the initial 600 s of immersion in Hank's solution. EIS was performed at an amplitude of 10 mV/SCE in the frequency range of 10^5-10^{-2} Hz. The EIS data were analyzed by curve fitting using ZSimpWin software. PDP tests were carried out with reference to the OCP at a sweep rate of 2 mV/s. The PDP curves were

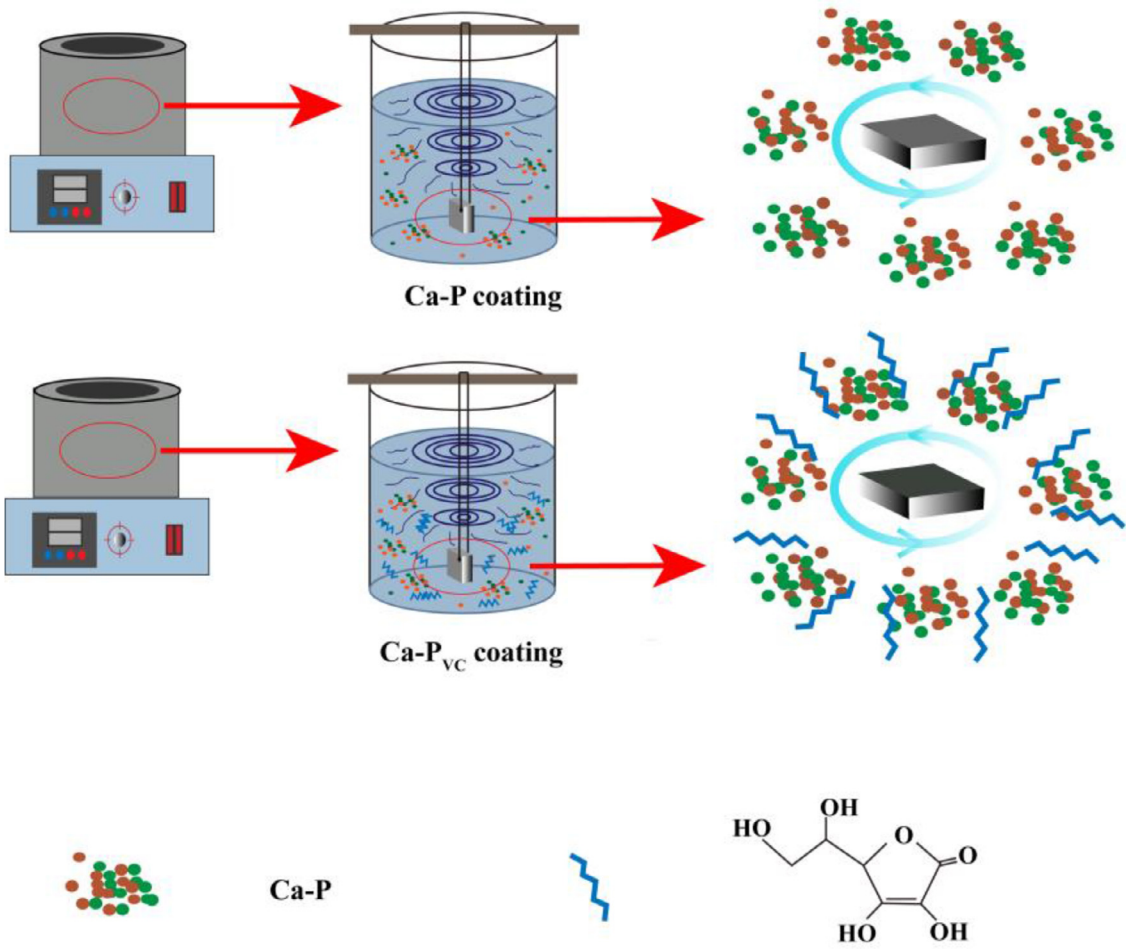

Fig. 1. Schematic illustrations of the preparation of the Ca-P coating and Ca-P_{VC} coating on Mg alloy AZ31.

analyzed by using Versatudio software. The polarization resistance (R_p) was calculated using the Stern Geary equation (Eq. (1)).

$$R_p = \beta_a\beta_c/\left(2.303i_{corr}\left(\beta_a+\beta_c\right)\right) \quad (1)$$

where i_{corr} is corrosion current density. β_a and β_c are the Tafel slope of anode and cathode, respectively.

The immersion tests were also used to evaluate the degradation rate of the uncoated and coated AZ31 Mg alloy samples. The samples were immersed in beakers and inverted funnels filled with Hank's solution, which were connected to a graduated burette. The Hank's solution was maintained at a temperature of 37.0 ± 0.5 °C and the solution level in the burette was intermittently measured per one hour for 168 h.

2.6. Biocompatibility tests

Mouse MC3T3-E1 pre-osteoblasts (Cell Bank, Chinese Academy of Sciences) were employed to investigate the cell toxicity of the samples. They were cultured in alpha-minimum Eagle's medium (α-MEM) supplemented with 10% fetal bovine serum (FBS) at 37 °C in a humidified atmosphere with 5% CO_2. Prior to the experiments, all the samples were sterilized by ultraviolet irradiation sterilization for 30 min. Thereafter, the extracts were prepared with a sample surface area to extraction medium (DMEM) ratio of 1 mL cm^{-2} in a humidified atmosphere with 5% CO_2 at 37 °C for 3 d. MC3T3-E1 cells and the α-MEM with 20% extracts and 10% FBS were cultured for 24 and 72 h. Thereafter, MTT (final concentration 0.5 mg/mL) was added into each well and incubated for a further 4 h. The absorbance was determined at 570 nm on a microplate spectrophotometer (Biotek). After being cultured for 24 and 72 h, live/dead staining experiments were employed to discern cell morphology and the cells were observed via a Confocal Laser Scanning Microscope (CLSM, LEICA DM6 B).

2.7. Statistical analysis

One-way analysis of variance (ANOVA) statistical analysis was performed to compare the cytocompatibility of cells cultured on different materials. The error bar means ± standard deviations: $p^* < 0.05$ and $p^{**} < 0.01$. The differences were considered statistically significant when $p^* < 0.05$ and $p^{**} < 0.01$. The error bar means ± standard deviations

3. Results

3.1. Surface analysis

Fig. 2(a-c) and (d-f) shows the SEM image of the synthesized Ca-P coating and Ca-P_{VC} coating, respectively. Interestingly, both the coatings exhibited bamboo leaf-like Ca-P particles. However, the Ca-P coating was neither uniform nor completely covered on the alloy substrate (Fig. 2(a)). The Ca-P particles were irregularly interlaced and exhibited different sizes (Fig. 2(b)). When VC was added to the Ca-P conversion bath, the Ca-P particles grew and covered the entire surface of the alloy surface. The Ca-P particles underwent growth in length and increase

in thickness (Fig. 2(e)), and thus exhibited a dense Ca-P_{VC} coating. As shown in Fig. 2, all the coatings contained C, O, Ca, and P, and a trace of Mg. In the Ca-P_{VC} coating, the Ca and P remained at a relatively higher level than the Ca-P only coating.

In general, the corrosion performance of the coated alloy is closely related to the interface bonding strength of the coating on the alloy substrate. The high bonding strength of the coating could prolong the service life of the alloy, which is critical for the successful applicant. The cross-section microstructures of the Ca-P and Ca-P_{VC} coatings are shown in Fig. 3. The thickness of Ca-P_{VC} coating was 10.00 ± 0.92 μm, about three times that of the Ca-P coating (3.00 ± 0.26 μm). For Ca-P_{VC} coating (Fig. 3(g) and (h)), the contents of the Ca and P were much higher than the Ca-P coating (Fig. 3(c) and (d)). Obviously, the addition of VC increased the thickness of the coating, which might facilitate an enhanced corrosion resistance.

Fig. 4 shows the three-dimensional (3D) surface topography images of Ca-P and Ca-P_{VC} coatings. To describe the influence of VC on the surface topography, mean line roughness (R_a) was used for characterization. More than 3 positions were selected for each sample to obtain an average value. The color codes (Fig. 4) indicate the surface roughness (i.e., R_a). The darker the color, the smaller the surface roughness [24]. As shown in Fig. 4, the R_a of the Ca-P coating and the Ca-P_{VC} coating was 3.14 ± 1.93 and 1.12 ± 0.12 μm, respectively. The Ca-P_{VC} coating was much smoother than the Ca-P coating, suggesting that the addition of VC reduces the roughness and improves the surface quality, which is in agreement with Figs. 2 and 3.

To evaluate the bonding strength of the coating to its substrate, scratch tests were conducted on the samples. It can be seen from Fig. 5 that Ca-P coating shows a poor bonding capacity as some tiny particles can be easily stripped from the surface using a small force. It would have been assigned a fractional rating of ASTM 4B for the Ca-P coating shown in Fig. 5(b). While only part of the coating from the cutting edge and adjacent intersections peeled off on the surface of the Ca-P_{VC} coating that its rating seemed to be ASTM 5B [25] (Fig. 5(e)), so the Ca-P_{VC} coating exhibited excellent adhesion. From the SEM morphology results, compared with the compact grains of the Ca-P_{VC} coating, the Ca-P coating was porous and covered with looser grains, thus confirming the Ca-P_{VC} coating already showed excellent adhesion.

Fig. 6(a) shows the FT-IR spectra of the Ca-P coating and Ca-P_{VC} coating. The characteristic bands at 3163-3488 cm^{-1} are attributed to O-H stretching [26,27]. A PO_4^{3-} absorption peak was observed on both coated samples in the 500-1200 cm^{-1} region, whereas the stretching vibration peaks of the PO_4^{3-} group were located at 1135, 1063, and 986 cm^{-1}, and the bending vibration absorption at 576 and 527 cm^{-1} peaks [28,29]. The intensity bands at 2360 and 529 cm^{-1} correspond to HPO_4^{2-} group [30]. The band at around 1650 cm^{-1} resulted from H_2O bending vibration [31], as well as the bands at around 874 cm^{-1} originated from CO_2 in H_2O [32]. As compared with the Ca-P coating, the Ca-P_{VC} coating showed a new absorption peak of the C=O group at 1724 cm^{-1} due to the contribution of VC [11]. These results demonstrated that the Ca-P_{VC} coating was successfully formed on the surface of the Mg alloy with the compounds of $CaHPO_4$ and HA ($Ca_{10}(PO_4)_6(OH)_2$).

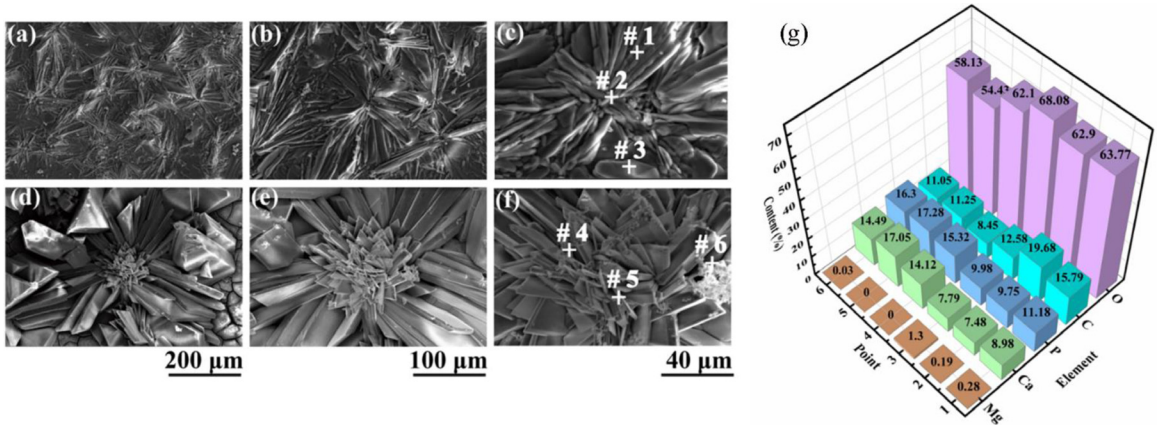

Fig. 2. SEM images of the (a-c) Ca-P and (d-f) Ca-P_{VC} coating, and (g) their EDS analysis, at.%.

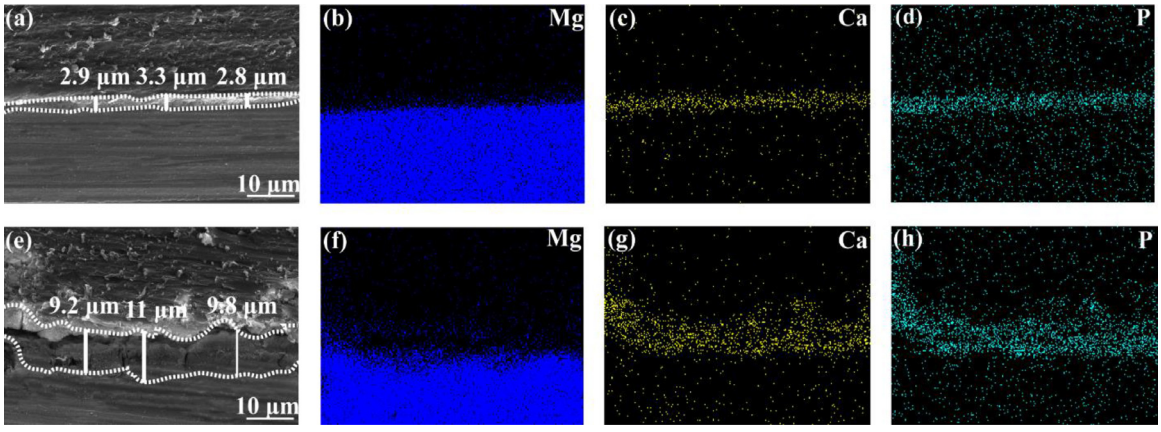

Fig. 3. Cross-sectional (a, e) and elemental mapping images (b-d, f-h) of the (a-d) Ca-P coating and (e-h) Ca-P_{VC} coating.

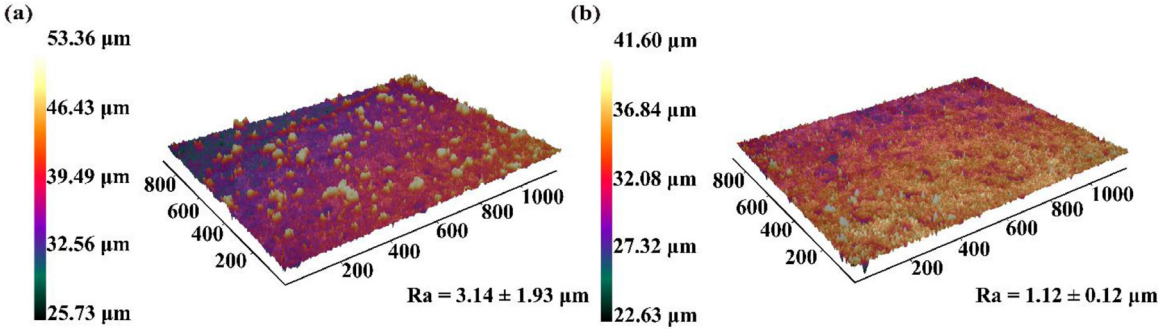

Fig. 4. Three-dimensional (3D) images of (a) Ca-P coating and (b) Ca-P_{VC} coating.

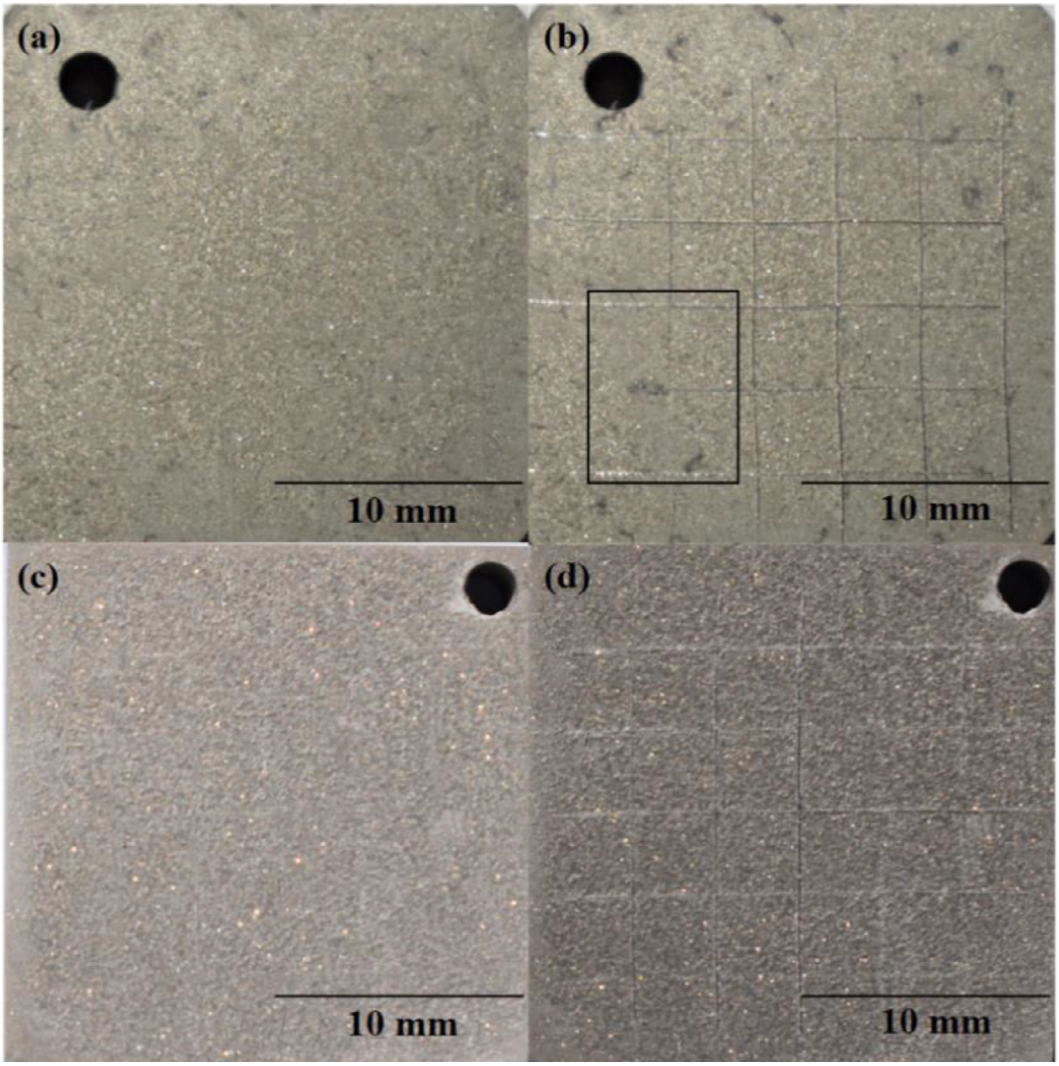

Fig. 5. (a, b) Ca-P coating and (c, d) Ca-P_{VC} coating samples (a, c) before and (b, d) after the scratching test.

Fig. 6(b) shows the XRD patterns of the Ca-P and Ca-P_{VC} coatings. As compared with the Ca-P coating, the inorganic phase composition of the Ca-P_{VC} coating changed significantly. The intensity of the characteristic peaks of Mg, DCPA ($CaHPO_4$) [33], and HA [34,35] phase increased. The Ca-P_{VC} coating mainly exhibited the diffraction peaks of the DCPA phase, which was consistent with the EDS results. The HA peaks were relatively weak, and may be the products of nanocrystals or amorphous crystallines. These results confirmed that the calcium phosphate coating was composed of DCPA and HA, which is consistent with the FT-IR analysis (Fig. 6(a)).

XPS analysis of the Ca-P_{VC} coating on the Mg alloy is presented in Fig. 7, where Fig. 7(a) depicts the whole range of the binding energy survey on the Ca-P_{VC} coating. The Ca-P_{VC} coating chemical compositions are in good agreement with the EDS data (Fig. 2(g)) results. As far as the C 1s spectra are concerned, they can be divided into three peaks. The C 1s spectra at 284.6 eV can be attributed to C-C/C-H bonding, and

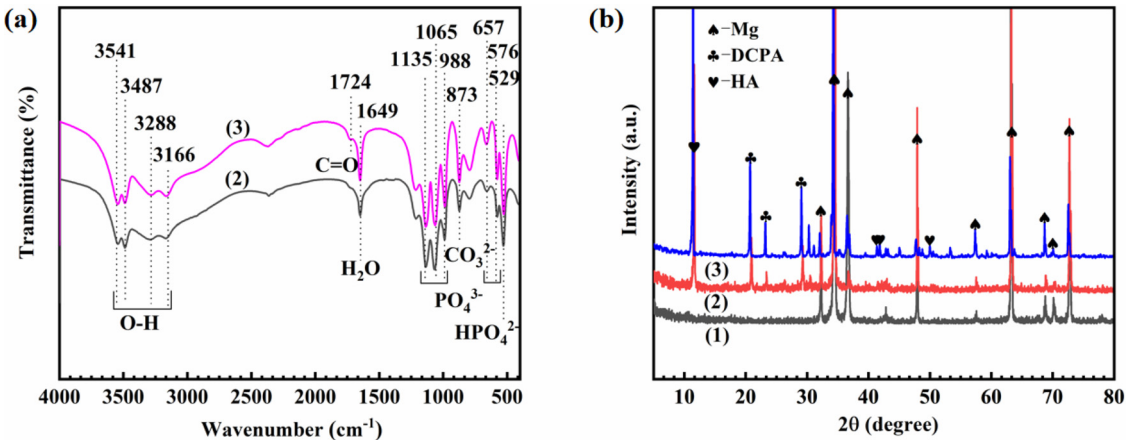

Fig. 6. (a) FT-IR spectra, (b) XRD patterns of the (1) Mg alloy AZ31, (2) Ca-P coating and (3) Ca-P_{VC} coating.

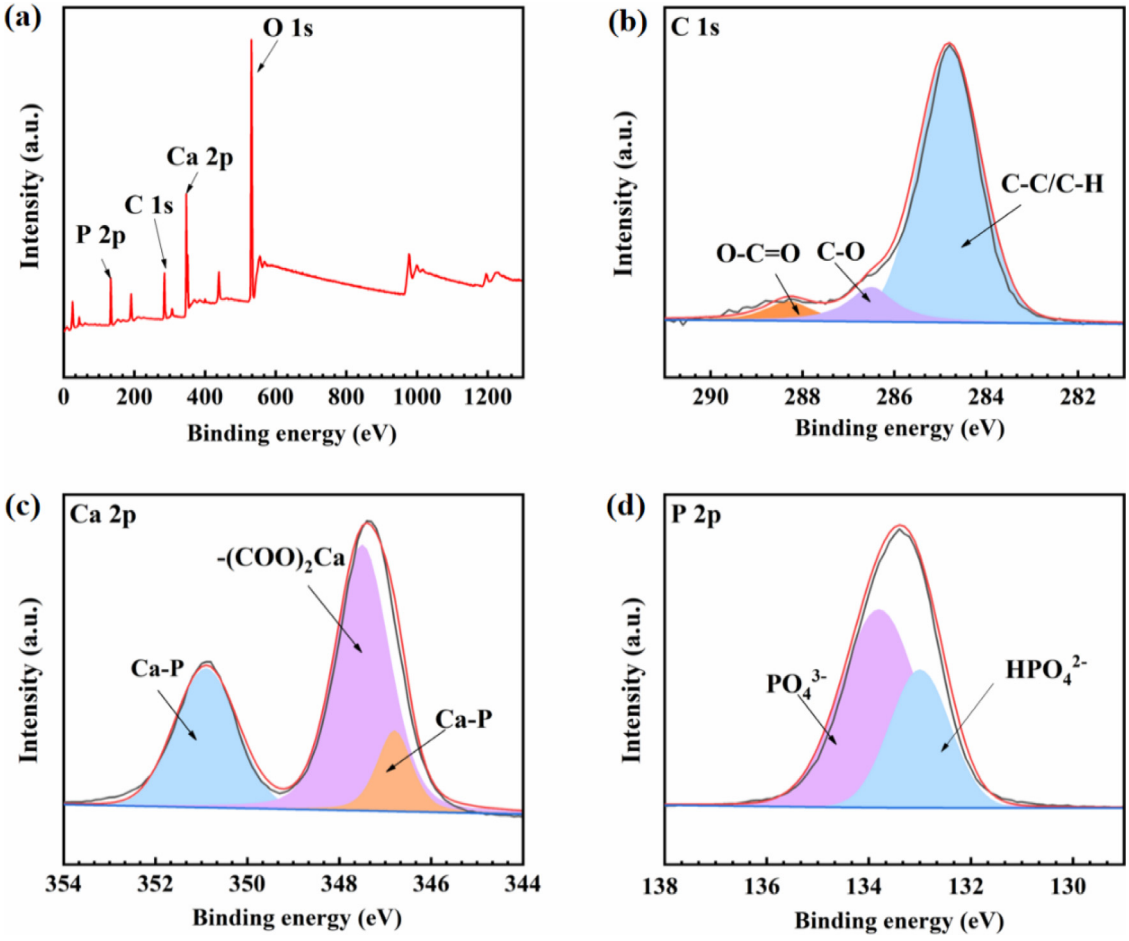

Fig. 7. (a) XPS survey plots and high-resolution spectra of (b) C 1s, (c) Ca 2p and (d) P 2p.

the peak at 286.9 eV is related to the presence of C-O bonding [32]; and, more importantly, the peak at 287.7 eV corresponds to the O-C=O group [36] (see Fig. 7(b)). It is worth noting that the presence of the C-C/C-H, C-O, and O-C=O groups was extremely strong, indicating that a large proportion of these groups may come from VC on the surface of Ca-P_{VC} coating. Also, Ca 2p and P 2p spectra of the Ca-P_{VC} coating were also included. Fig. 7(c) exhibits the presence of -$(COO)_2$Ca peaks in the sample surface, revealing that the transformation of VC into L-TA might be the key point for promoting the deposition of Ca-P coating. The nucleation of Ca-P coating on the Mg alloy surface was greatly facilitated by the coordination of the L-TA molecule with Ca^{2+}. The two peaks at 346.8 and 350.5 eV were detected in addition to the peak at 347.4 eV, which were assigned to Ca-P chemical bonds. According to the P 2p spectrum, P was derived from HPO_4^{2-} (347.8 eV) and PO_4^{3-}

(346.9 eV) in Ca-P_{VC} coating (Fig. 7(d)) [20]. Based on these results (Fig. 7(c) and (d)), it can be concluded that chemical bonds were formed between Ca^{2+}, HPO_4^{2-} and PO_4^{3-}. The complexation of L-TA (contain carboxylic group (-COOH)), and hereby, Ca^{2+} potentially promotes the deposition of calcium and phosphorus products on the surface of the Mg alloys. The XPS analysis demonstrated that -COOH group from L-TA molecules played a dominant role in the formation of the Ca-P_{VC} coating.

3.2. Corrosion behavior

To evaluate the corrosion resistance of the different coatings, electrochemical measurements of bare alloy, Ca-P coated alloy, and Ca-P_{VC} coated alloy in Hank's solution were performed. The PDP curves are shown in Fig. 8 and the corresponding parameters are presented in Table 1. The Ca-P_{VC} coated sample presented the minimum i_{corr} value of 1.36×10^{-6} A cm^{-2}, which decreased one order of magnitude in comparison to that of the bare Mg alloy; whereas, the Ca-P coated alloy showed an i_{corr} value of 2.85×10^{-6} A cm^{-2}. The R_p values calculated are arranged in the following order: Bare AZ31 Mg alloy (2.14×10^3 Ω cm^2) < Ca-P coated alloy (1.75×10^4 Ω cm^2) < Ca-P_{VC} coated alloy (4.48×10^4 Ω cm^2), which suggest that the Ca-P_{VC} coating is more protective than the Ca-P coating. The SEM analysis (Fig. 2(a)) revealed that the highly dense Ca-P_{VC} coating acted as an excellent physical barrier to any penetration of the aggressive ions.

The Nyquist plots of the bare and the coated samples are shown in Fig. 9. It can be noticed that the diameter of the semicircle increased in the following order: AZ31 Mg alloy < single Ca-P coating < Ca-P_{VC} coating (Fig. 9(a)). The equivalent circuit presented in Fig. 9(c)-(e) corresponds to the EIS data of AZ31 Mg alloy, Ca-P coated alloy, and Ca-P_{VC} coated alloy, respectively, where R_s represents solution resistance; CPE_1 and CPE_2 indicate constant phase angle components; R_{ct} is the charge transfer resistance; R_L and L refer to inductive resistance and inductance, respectively; R_1 is the coating resistance [37,38]. For AZ31 Mg alloy substrate and Ca-P coated samples, the impedance spectra exhibited high- and medium-frequency capacitance loops followed by low-frequency inductor loops. Literature suggests that the high-frequency capacitive loop is from both charge transfer and film effect of corrosion products, the medium-frequency capacitive loop is usually associated with relaxation of mass transport and accumulation of corrosion products, and, the low-frequency inductive loop is ascribed to the relaxation processes of adsorbed intermediates of the corrosion process [39] (see Fig. 9(c) and (d)). The R_L of Ca-P coating was 5.71×10^3 Ω cm^2, whereas the R_L of AZ31 Mg alloy was only 2.91×10^3 Ω cm^2. As far as the Ca-P_{VC} coating was concerned, it was no inductor in the low-frequency region, demonstrating that the coating was maintained completeness and shielded the substrate as a barrier. Currently, the larger the R_{ct} value, the better the corrosion resistance [40]. According to Table 2, the R_{ct} value for the Ca-P_{VC} coating (2.47×10^4 Ω cm^2) was higher than that of the Ca-P

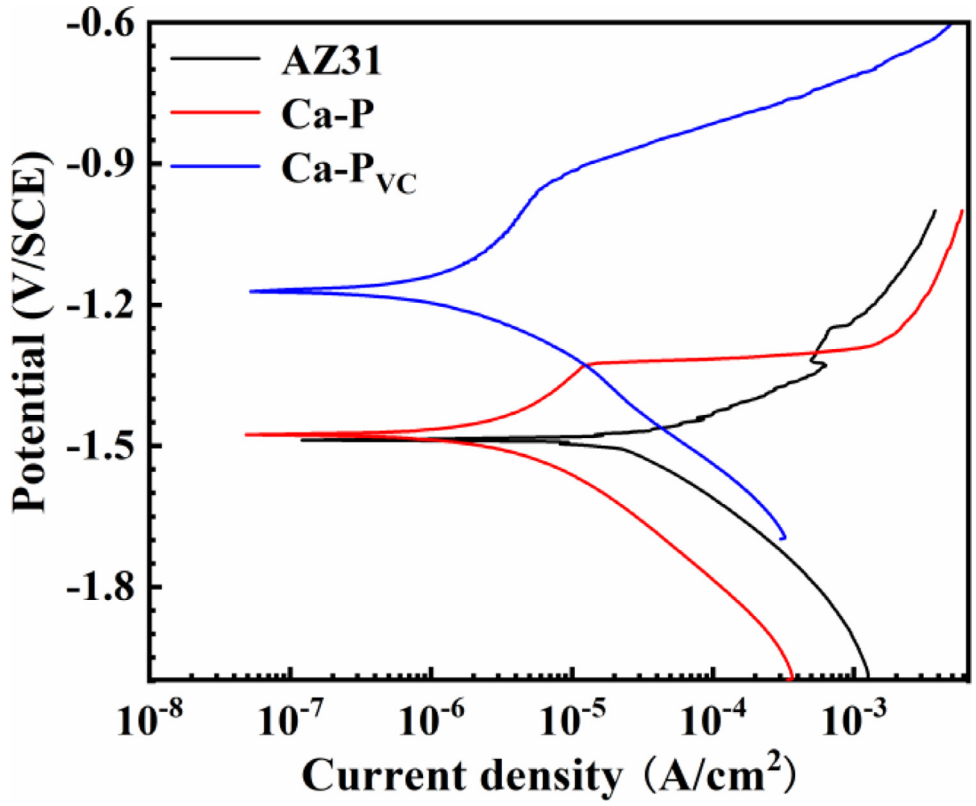

Fig. 8. PDP curves of the Mg alloy AZ31, Ca-P coating and Ca-P_{VC} coating.

Table 1
EIS analysis of the AZ31 Mg alloy, Ca-P coating & Ca-P_{VC} coating.

Sample	E_{corr} (V/SCE)	i_{corr} (A cm^{-2})	β_a (mV dec^{-1})	$-\beta_c$ (mV dec^{-1})	R_p (Ω cm^2)
AZ31	-1.48	1.73×10^{-5}	258.19	127.67	2.14×10^3
Ca-P	-1.48	2.85×10^{-6}	219.32	195.34	1.75×10^4
Ca-Pvc	-1.18	1.36×10^{-6}	532.21	190.38	4.48×10^4

coating (5.78×10^3 Ω cm^2) and much higher than that of the AZ31 Mg alloy substrate (1.66×10^2 Ω cm^2). In addition, in Fig. 9(b) the $|Z|$ values could be ordered as follows: Mg alloy AZ31 < Ca-P coating < Ca-P_{VC} coating. The EIS results were in good agreement with the PDP results. Thus, it can be concluded that Ca-P_{VC} coating provides better protection for the substrate as compared to Ca-P coating.

The corrosion resistance of the samples was also investigated via hydrogen evolution rates in different exposure time in Hank's solution. The corrosion rates and pH values of AZ31 Mg alloy, Ca-P, and Ca-P_{VC} coated samples are plotted in Fig. 10. During the initial 24 h immersion, there was a rapid increase in pH value and a decrease in the hydrogen evolution rate. After nearly 100 h immersion, the deposition of calcium phosphate and magnesium phosphate during the corrosion process of the samples slowed down the degradation rate of the Mg alloy. It was clearly evident that the Ca-P_{VC} coated alloy had the best corrosion resistance, followed by the Ca-P coated alloy in comparison with the AZ31 Mg alloy. The Ca-P coating had limited corrosion protection due to its thin and loose structure. While the Ca-P_{VC} coating on the surface of Mg

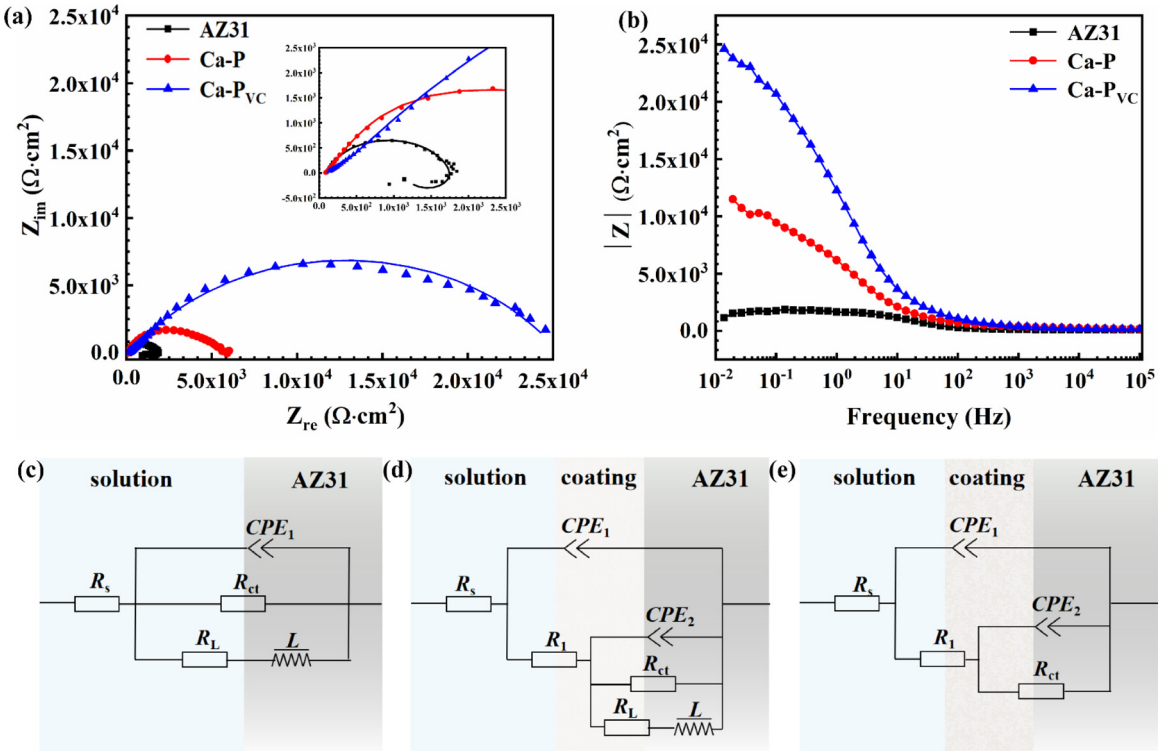

Fig. 9. (a) Nyquist and (b) Bode plots of the Mg alloy AZ31, Ca-P coating and Ca-P_{VC} coating; equivalent circuits of the (c) Mg alloy AZ31, (d) Ca-P coating and (e) Ca-P_{VC} coating.

Table 2
EIS analysis of the Mg alloy AZ31, Ca-P coating & Ca-P_{VC} coating.

Sample	R_s (Ω cm^2)	CPE_1 (Ω^{-1} cm^{-2}•s^{-1})	n_1	R_1 (Ω cm^2)	CPE_2 (Ω^{-1} cm^{-2} s^{-1})	n_2	R_{ct} (Ω cm^2)	R_L (Ω cm^2)	L (H cm^2)
Mg alloy AZ31	100.10	1.75×10^{-5}	0.85	-	-	-	2.66×10^2	2.91×10^3	3.39×10^4
Ca-P coating	86.31	4.84×10^{-5}	0.68	0.57	4.22×10^{-5}	0.81	5.78×10^3	5.71×10^3	209.70
Ca-P_{VC} coating	114.70	9.28×10^{-6}	0.65	4.92	8.69×10^{-6}	0.63	2.47×10^4	-	-

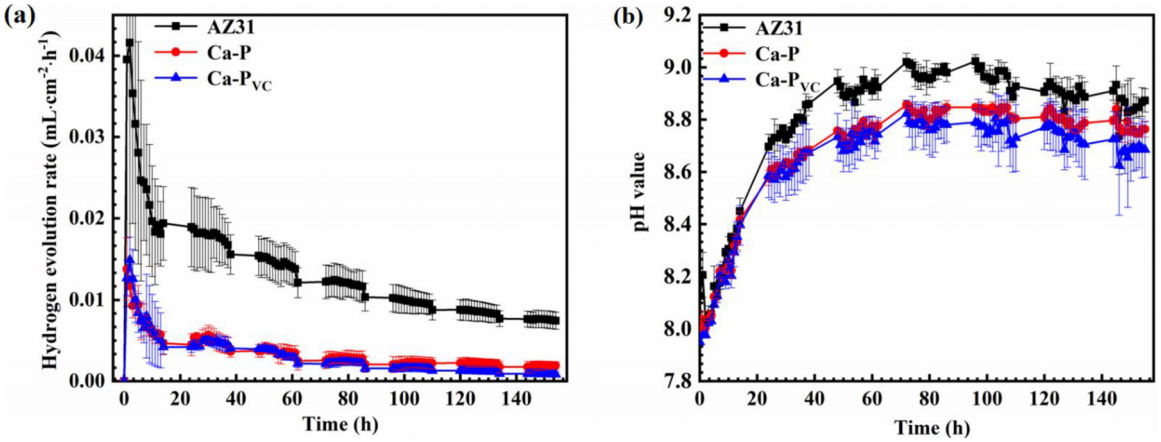

Fig. 10. (a) Hydrogen evolution rates and (b) pH-time curves of the Mg alloy AZ31, Ca-P coating and Ca-P_{VC} coating.

alloy sealed its porous surface thus preventing corrosive ions from penetrating through the coating.

Macroscopic images are shown in Fig. 11(a, e, i), indicating that AZ31 Mg alloy has undergone severe corrosion and Ca-P coated alloy exhibited a large corrosion pit, whereas the Ca-P_{VC} coating did not show any significant damage during the 14 d immersion in Hank's solution. Higher magnification SEM images reveal corrosion products accumulation on the surface of AZ31 Mg alloy along with numerous cracks [41]. Even the Ca-P coating exhibited cracks which could be due to the thin and uneven coating. The cracks served as channels for the penetration of corrosive ions, such as chloride ions, through the coating [42] and resulted in large size corrosion pits. However, the Ca-P_{VC} coated alloy did not show any corrosion attack. Thus, the Ca-P_{VC} coating can provide relatively longer corrosion protection to AZ31 Mg alloy.

The chemical compositions of the degraded samples were analyzed using EDS. Fig. 11(m) shows that the main elements on the surface of the samples are C, O, Mg, Ca, and P. When comparing with the composition of the original samples (Fig. 2(g)), the content of Ca and P elements has increased significantly after 14 d of immersion in Hank's solution, which indicates that the granular precipitations on the surface are rich in Ca and P. In the case of Ca-P_{VC} coating, most of the Ca and P were from the Ca-P coating and remained at a relatively high level, whereas for Ca-P coating, the Ca and P contents were lower than that of Ca-P_{vc} coating. Also, the Ca and P contents in the corrosion products formed on AZ31 Mg alloy were much lower than that of the Ca-P_{VC} coating.

Fig. 12(a) shows the FT-IR spectra of AZ31 Mg alloy, Ca-P coating, and Ca-P_{VC} coating after being immersed in Hank's solution for 168 h. The absorption bands at 3541 and 3487 cm^{-1} can be attributed to the tensile vibration of O-H, indicating the formation of $Mg(OH)_2$ corrosion product. The adsorption peak centered at 1649 cm^{-1} is ascribed to the O-H bending vibration of the water molecules [43]. The CO_3^{2-} absorption peaks (1433 and 873cm^{-1}) are the result of the reaction between OH^- and CO_2 in the air [44,45]. The adsorption peaks at 1374 and 526 cm^{-1} are assigned to the HPO_4^{2-} stretching vibration. The presence of strong peaks at 1065 and 576 cm^{-1} is considered to be for PO_4^{3-} groups. The peaks at 1135 cm^{-1} (Ca-P and Ca-P_{VC} coatings) are also the PO_4^{3-} group [46]. Fig. 12(b) shows the XRD patterns of the samples after 168 h of immersion in Hank's solution. Interestingly, the inorganic phase composition of the samples did not change after immersion. For these samples, the primary corrosion product was $Mg(OH)_2$ with a small amount of Ca-P compounds (e.g. HA and DCPA) [47].

Fig. 13(a-h) exhibits the Live/Dead staining of MC3T3-E1 cells after an incubation of 24 and 72 h. The cells on all the samples exhibited generally healthy fusiform-like shape, and widely spreading with respect to morphology, which indicates an acceptable and enhanced cytocompatibility to osteoblasts. The cytotoxicity of the samples was determined using MC3T3-E1 cells and an MTT assay, as shown in Fig. 13(i). It can be seen that the cell viability of all the samples was less than 100% after 24 and 72 h of culture. Interestingly, the Ca-P_{VC} coated alloy exhibited higher cell viability than the AZ31 Mg substrate and Ca-P coating after 72 h of culture. The viability of the cells with the AZ31 Mg substrate and Ca-P coated alloy declined to some extent, but remained above 75%, which is acceptable for cellular applications [48,49]. The improved cellular compatibility of Ca-P_{VC} coating can be ascribed to the combination of VC and Ca^{2+} in the Ca-P_{VC} coating, which promoted the formation of hydroxyapatite and improved the corrosion resistance of Mg alloys.

4. Discussion

4.1. Comparison of corrosion resistance of different coatings

Fig. 14 compares the corrosion resistance performance of the coatings, and it is clearly evident that the coatings have significantly improved the corrosion resistance of the alloy.

Li et al. [50] reported that the glucose-induced composite coating acted as a protective film against corrosion of Mg immersed in Hank's solution over a long time. Interestingly, it was observed that the composite coating provided corrosion protection during the initial period and also induced precipitation of Ca-P to form a dense layer on the coated surface. It was suggested that glucose ($CH_2OH(CHOH)_4CHO$) changes into gluconic acid ($CH_2OH(CHOH)_4COOH$), which was beneficial in concentrating Ca^{2+} on the Mg surface owing to the chelation of gluconic acid with Ca^{2+}. Notably, the i_{corr} of the Ca-P composite coating (6.79×10^{-6} A cm^{-2}) induced by glucose decreased an order of magnitude as compared with that of the pure Mg substrate (2.36×10^{-5} A cm^{-2}) (see Fig. 14(a)), and its R_{ct} (2309.0 Ω cm^2) increased by more than 5 times than that of the pure Mg substrate (409.5 Ω cm^2) (see Fig. 14(b)).

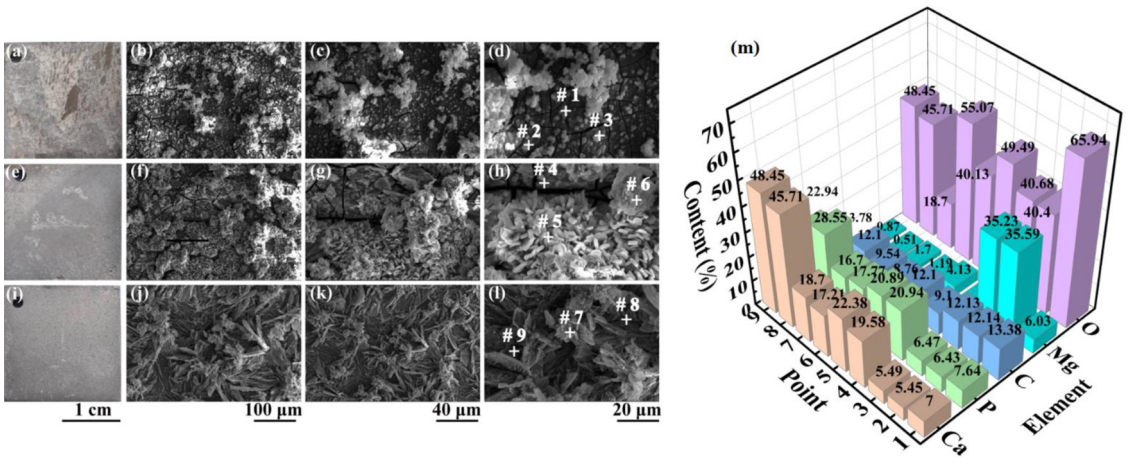

Fig. 11. Digital camera photographs, SEM morphologies for the (a-d) Mg alloy AZ31, (e-h) Ca-P coating and (i-l) Ca-P_{VC} coating after the immersion for 168 h and (m) the EDS analysis result.

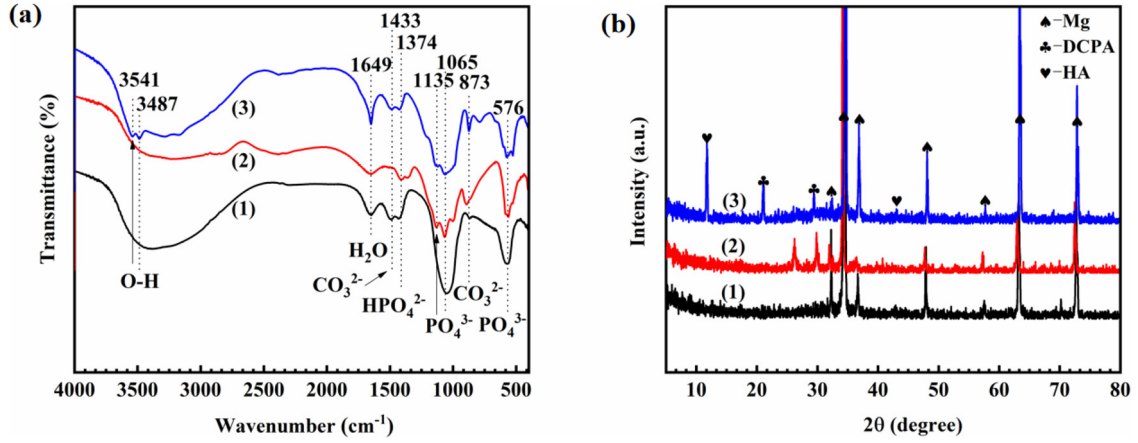

Fig. 12. (a) FT-IR spectra, (b) XRD patterns after 168 h immersion of the (1) Mg alloy AZ31, (2) Ca-P coating and (3) Ca-P_{VC} coating.

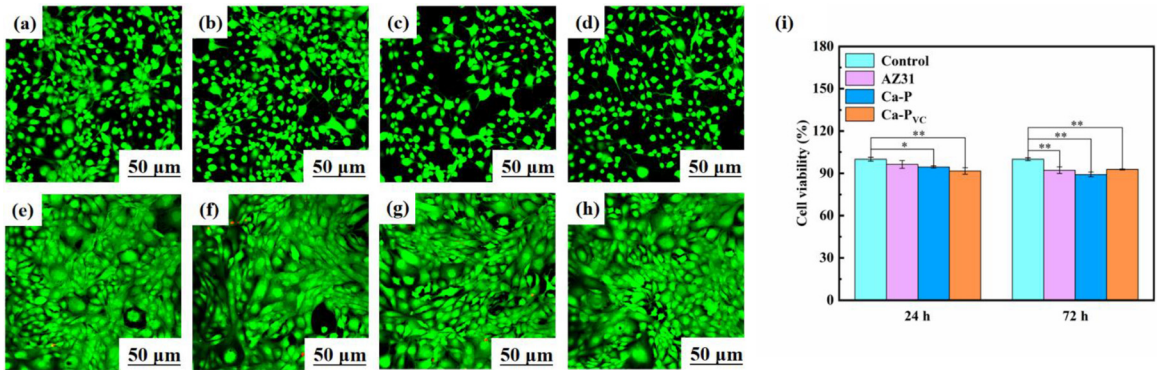

Fig. 13. CLSM images of MC3T3-E1 after culturing for 24 and 72 h in extracts of the (a, e) negative control, (b, f) AZ31 substrate, (c, g) Ca-P and (d, h) Ca-PVC coatings; (i) viability of MC3T3-E1 cells incubated for 24 and 72 h of negative control, AZ31 substrate, Ca-P and Ca-P_{VC} coatings (Statistically differences at $p^{*} < 0.05$ vs. control, statistically significant differences at $p^{**} < 0.01$ vs. control).

To clarify the influence of amino acid groups on film formation, Wang et al. [51] probed the formation mechanisms of phenylalanine (Phe), methionine (Met), and asparagine (Asn) additive-induced Ca-P coatings on AZ31 Mg alloy. The adsorption of the amino group was mainly achieved through the coupling of the lone pair electrons of nitrogen atoms with the Mg surface, whereas the carboxyl group was attached with Mg^{2+} via their oxygen atoms. Additionally, the heteroatoms in the amino acids share their lone pair electrons with the vacant molecular orbitals of Mg. It can be noted that the i_{corr} of Ca-$P_{Phe/Met/Asn}$ coating is an order of magnitude lower than that of AZ31 Mg alloy. The i_{corr} values of the samples can be arranged in the following decreasing order: AZ31 Mg alloy (1.73×10^{-5} A cm^{-2}) > Ca-P coating (6.54×10^{-6} A cm^{-2}) > Ca-$P_{Phe/Met/Asn}$ coating (2.71×10^{-6} A cm^{-2}). Also, the R_{ct} values can be arranged in the following order: AZ31 Mg alloy (578.5 Ω cm^2) < Ca-P coating (593.8 Ω cm^2) < Ca-$P_{Phe/Met/Asn}$ coating (7761.0 Ω cm^2). These results indicate that the amino acid-induced Ca-P coating provides good corrosion protection for the substrate.

Fan et al. [52] prepared Ca-$P_{L\text{-}Cys}$ coating on the surface of AZ31 Mg alloy using a hydrothermal method, i.e., utilizing L-Cysteine (L-Cys), which has better biocompatibility and biodegradability in the human physiological environment. L-Cys is covalently fixed on the surface of Mg alloy through chelating reactions with OH^- and PO_4^{3-}, while the -COOH group interacted with Ca^{2+} and enhanced the coating performance. The i_{corr} of Ca-$P_{L\text{-}Cys}$ coating (6.61×10^{-7} A cm^{-2}) was two orders of magnitude lower than that of AZ31 Mg alloy (1.65×10^{-5} A cm^{-2}), and the R_{ct} of Ca-$P_{L\text{-}Cys}$ coating was far higher than that of AZ31 Mg alloy substrate, as shown in Fig. 14.

In the case of VC, it was rapidly air-oxidized and decomposed to dehydroascorbic acid, which was further transformed into L-TA. The present study confirms that the carboxyl group (-COOH) in the molecular structure of L-TA interacts with Ca^{2+}, and the ions were trapped in the solution/substrate interface during the formation of the coating. From the electrochemical results, it was seen that the i_{corr} of the Ca-P_{VC} coating was about 1.36×10^{-6} A/cm^2, which showed the lowest i_{corr} as compared with the Ca-P coating (2.85×10^{-6} A cm^{-2}) and AZ31 Mg alloy substrate (1.73×10^{-5} A cm^{-2}). Similarly, the R_{ct} of the Ca-P_{VC} coating has been significantly improved the corrosion resistance of the alloy.

The corrosion resistance (based on i_{corr} values) of the Ca-P_{VC} coating was better than that of the glucose-induced Ca-P coating and equivalent to the corrosion resistance of the Ca-P coating induced by a variety of amino acids. However, the results of R_{ct} revealed that the Ca-P_{VC} coating had the highest value of charge transfer resistance (see Fig. 14). Therefore, it can be confirmed that the addition of VC can provide good corrosion-resistant. Glucose was converted into gluconic acid in solution, which contains -COOH group with strong polarity, and amino acids contain -NH_2, -COOH, and -SH groups, whereas VC and its decomposition products with functional groups containing oxygen that have the ability to form complexes with metal ions. These studies indicate that the functional groups in the corrosion inhibitors were essential for achieving good corrosion resistance properties.

4.2. Formation mechanism of the Ca-P_{VC} coating

Fig. 15 illustrates the reaction mechanisms of the Ca-P_{VC} coating. In the initial stage of the coating formation, dissolution of AZ31 Mg alloy releases a large number of Mg^{2+} which react with OH^- to form $Mg(OH)_2$ precipitates on the surface of the alloy Eqs. (2) to ((4)).

In the second stage, the VC crystal is stable in air, but the solution of VC is rapidly air-oxidized and decomposes to dehydroascorbic acid (Eq. (5)) [53]. Then it decomposes into L-Threonic acid and oxalic acid in the solution over pH 4 as shown in Eq. (6). Moreover, it has been demonstrated that VC is stable at 10 °C, but the decomposition of VC is promoted above 20 °C [54], and this experiment was conducted in the solution at 60 °C. It should be noted that L-Threonic acid is a major breakdown product of VC. In the process of coating formation, the carboxyl group (-COOH) [55] in the molecular structure of L-Threonic acid forms a complex with Ca^{2+}, which traps Ca^{2+} at the solution/substrate interface resulting in an increase in the concentration of Ca^{2+} and promoting the formation of Ca-P coating at the interface Eqs. (9) and ((10)).

In addition, the attraction electrostatically among the spatial distributed Ca^{2+}, HPO_4^{2-}, PO_4^{3-}, and OH^- in the vicinity of the interface was more powerful, which adequately guaranteed the growth of Ca-P coatings. Ultimately, a dense and suitable thickness of DCPA and HA coatings is successfully formed (Fig. 14).

$$Mg \rightarrow Mg^{2+} + 2e^- \quad (2)$$

$$2H_2O + 2e^- \rightarrow 2OH^- + H_2\uparrow \quad (3)$$

$$Mg^{2+} + OH^- \rightarrow Mg(OH)_2\downarrow \quad (4)$$

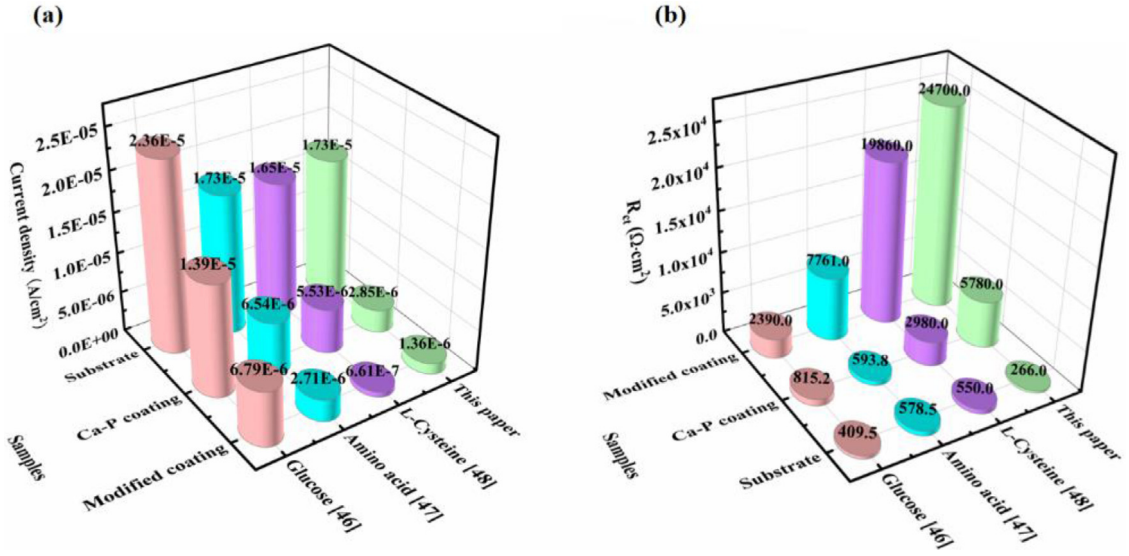

Fig. 14. Comparison of (a) corrosion current density (i_{corr}) and (b) charge transfer resistance (R_{ct}) of different modified coatings.

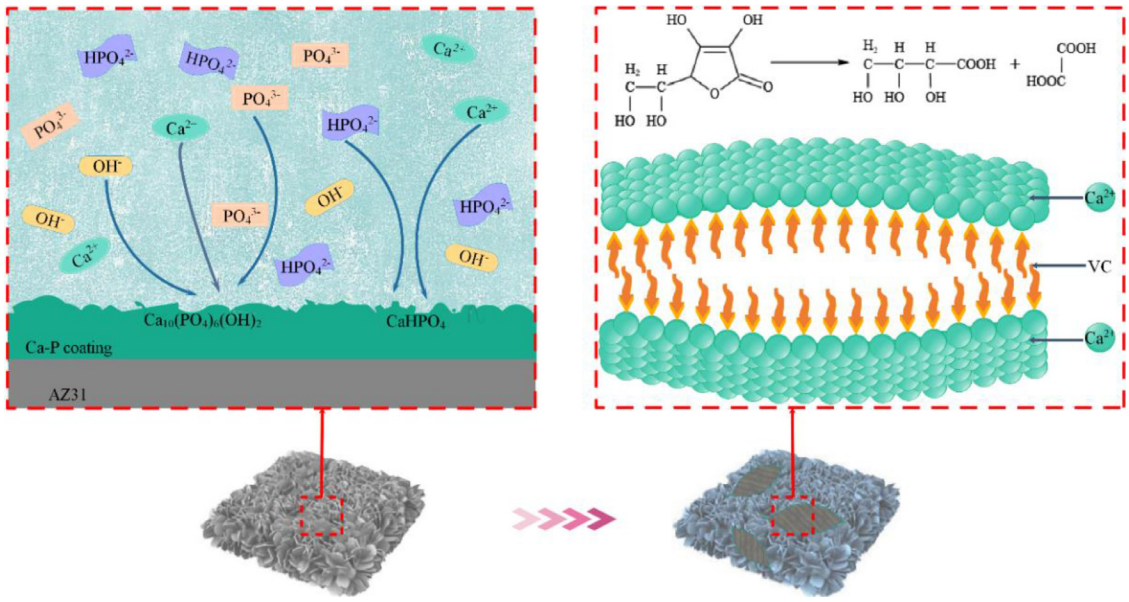

Fig. 15. Schematic diagram of the formation mechanism of the Ca-P_{VC} coating.

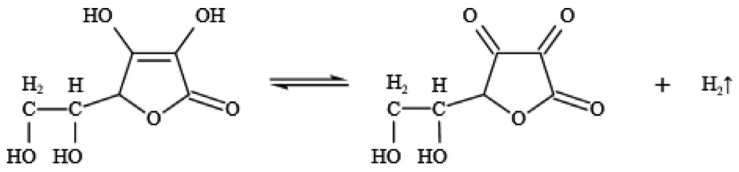

(5)

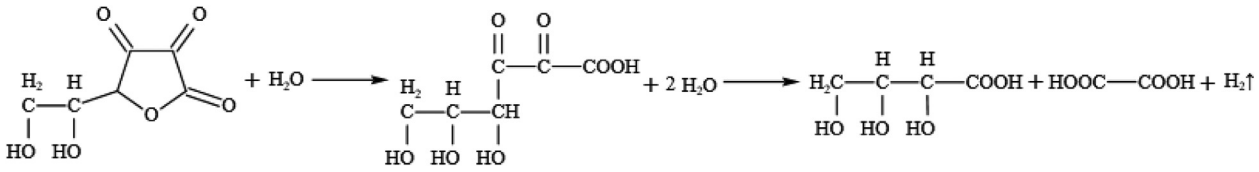

(6)

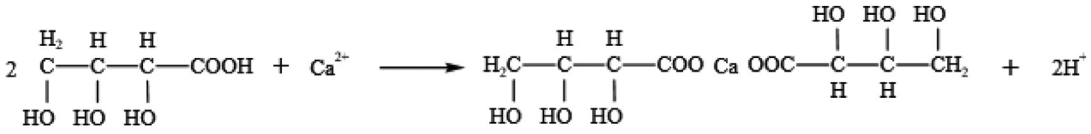

(7)

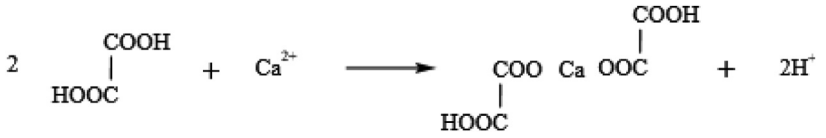

(8)

$$Ca^{2+} + HPO_4{}^{2-} \rightarrow CaHPO_4 \quad (9)$$

$$10Ca^{2+} + 8OH^- + 6HPO_4{}^{2-} \rightarrow Ca_{10}(PO_4)_6(OH)_2 + 6H_2O \quad (10)$$

5. Conclusions

(1) In this study, a highly dense Ca-P_{VC} coating was synthesized on AZ31 Mg alloy by chemical conversion treatment. The average thickness of the Ca-P_{VC} coating (10.00 ± 0.92 μm) was significantly higher than that of the Ca-P coating (3.00 ± 0.26 μm). Meanwhile, the mean line roughness of the Ca-P_{VC} coating (1.12 ± 0.12 μm) was significantly lower than that of the Ca-P coating in absence of VC (3.14 ± 1.93 μm). Further, the Ca-P_{VC} coating presented a better bonding strength than the Ca-P coating. These observations suggest that VC promoted the nucleation process of the Ca-P coating, resulting in a significant increment in coating thickness, density, and bonding strength.

(2) The Ca-P_{VC} coating microstructure exhibited bamboo leaf-like crystals. The electrochemical measurements indicated that Ca-P_{VC} coating possesses a good corrosion resistance with high R_{ct} (2.47×10^4 Ω cm^2), and low i_{corr} (1.36×10^{-6} A cm^{-2}). In particular, VC is transformed into L-Threonic acid and oxalic acid with ionization groups (carboxyl), which induces the Mg surface to be negatively charged. Thus, The adsorption of VC on the surface of the alloy was beneficial for the accumulation of Ca^{2+}.

(3) In vitro immersion test results show that the Ca-P_{VC} coating facilitates hydroxyapatite formation and increases the corrosion protection of the alloy. The hydrogen evolution rate was also low with Ca-P_{VC} coating confirming its increased protection against corrosion of the alloy. The cytotoxicity test results showed enhanced cytocompatibility to osteoblasts. Hence, this study suggests that Ca-P_{VC} coating has a great potential for Mg-based biodegradable biomaterials.

Acknowledgment

This work was financially supported by the National Natural Science Foundation of China (No. 52071191).

References

[1] J. Song, J. She, D. Chen, F. Pan, Latest research advances on magnesium and magnesium alloys worldwide, J. Magnes. Alloy. 8 (2020) 1–41.
[2] Z.Z. Yin, W.C. Qi, R.C. Zeng, X.B. Chen, C.D. Gu, S.K. Guan, Y.F. Zheng, Advances in coatings on biodegradable magnesium alloys, J. Magnes. Alloy. 8 (2020) 42–65.
[3] Y. Yang, X. Xiong, J. Chen, X. Peng, D. Chen, F. Pan, Research advances in magnesium and magnesium alloys worldwide in 2020, J. Magnes. Alloy. 9 (2021) 705–747.
[4] R.C. Zeng, F. Zhang, Z.D. Lan, H.Z. Cui, E.H. Han, Corrosion resistance of calcium-modified zinc phosphate conversion coatings on magnesium–aluminium alloys, Corros. Sci. 88 (2014) 452–459.
[5] L.Y. Cui, G.B. Wei, Z.Z. Han, R.C. Zeng, L. Wang, Y.H. Zou, S.Q. Li, D.K. Xu, S.K. Guan, In vitro corrosion resistance and antibacterial performance of novel tin dioxide-doped calcium phosphate coating on degradable Mg-1Li-1Ca alloy, J. Mater. Sci. Technol. 35 (2019) 254–265.
[6] M.B. Kannan, Electrochemical deposition of calcium phosphates on magnesium and its alloys for improved biodegradation performance: A review, Surf. Coat. Technol. 301 (2016) 36–41.
[7] C. Ke, Y.J. Wu, Y. Qiu, J.H. Duan, N. Birbilis, X.B. Chen, Influence of surface chemistry on the formation of crystalline hydroxide coatings on Mg alloys in liquid water and steam systems, Corros. Sci. 113 (2016) 145–159.
[8] M.P. Brady, W.J. Joost, C.David Warren, Insights from a recent meeting: current status and future directions in magnesium corrosion research, Corrosion 73 (2017) 452–462.
[9] M.S. Song, R.C. Zeng, Y.F. Ding, R.W. Li, M. Easton, I. Cole, N. Birbilis, X.B. Chen, Recent advances in biodegradation controls over Mg alloys for bone fracture management: A review, J. Mater. Sci. Technol. 35 (2019) 535–544.
[10] D. Kumar, N. Jain, V. Jain, B. Rai, Amino acids as copper corrosion inhibitors: A density functional theory approach, Appl. Surf. Sci. 514 (2020) 145905.
[11] L. Valek, S. Martinez, D. Mikulić, I. Brnardić, The inhibition activity of ascorbic acid towards corrosion of steel in alkaline media containing chloride ions, Corros. Sci. 50 (2008) 2705–2709.
[12] L. Feng, Y.W. Zhang, C. Wen, S.Z. Li, J.F. Li, D. Cheng, J.Y. Bai, Q.X. Cui, L.G. Zhang, Effect of initial deposition behavior on properties of electroless Ni–P coating on ZK60 and ME20 magnesium alloys, Trans. Nonferrous Met. Soc. 31 (2021) 2307–2322.
[13] H. Wang, Y. Song, D. Shan, E.-H. Han, Effects of corrosive media on the localized corrosion forms of Mg-3Zn alloy, Corros. Commun. 2 (2021) 24–32.

[14] L.M. Calado, M.G. Taryba, Y. Morozov, M.J. Carmezim, M.F. Montemor, Novel smart and self-healing cerium phosphate-based corrosion inhibitor for AZ31 magnesium alloy, Corros. Sci. 170 (2020) 108648.
[15] P. Zhou, L. Yang, Y. Hou, G. Duan, B. Yu, X. Li, Y. Zhai, B. Zhang, T. Zhang, F. Wang, Grain refinement promotes the formation of phosphate conversion coating on Mg alloy AZ91D with high corrosion resistance and low electrical contact resistance, Corros. Commun. 1 (2021) 47–57.
[16] L.Y. Ling, L.Y. Cui, R.C. Zeng, S.Q. Li, X.B. Chen, Y.F. Zheng, M.Bobby Kannan, Advances in functionalized polymer coatings on biodegradable magnesium alloys-A review, Acta Biomater. 79 (2018) 23–36.
[17] W. Yan, Y.J. Lian, Z.Y. Zhang, M.Q. Zeng, Z.Q. Zhang, Z.Z. Yin, L.Y. Cui, R.C. Zeng, In vitro degradation of pure magnesium-the synergetic influences of glucose and albumin, Bioact. Mater. 5 (2020) 318–333.
[18] Z.Q. Zhang, L. Wang, M.Q. Zeng, R.C. Zeng, M.B. Kannan, C.G. Lin, Y.F. Zheng, Biodegradation behavior of micro-arc oxidation coating on magnesium alloy-from a protein perspective, Bioact. Mater. 5 (2020) 398–409.
[19] C.Y. Li, X.L. Fan, R.C. Zeng, L.Y. Cui, S.Q. Li, F. Zhang, Q.K. He, M.B. Kannan, H.W. Jiang, D.C. Chen, S.K. Guan, Corrosion resistance of in-situ growth of nano–sized $Mg(OH)_2$ on micro-arc oxidized magnesium alloy AZ31—Influence of EDTA, J. Mater. Sci. Technol. 35 (2019) 1088–1098.
[20] Y. Wang, B.H. Ding, S.Y. Gao, X.B. Chen, R.C. Zeng, L.Y. Cui, S.J. Li, S.Q. Li, Y.H. Zou, E.H. Han, S.K. Guan, Q.Y. Liu, In vitro corrosion of pure Mg in phosphate buffer solution—Influences of isoelectric point and molecular structure of amino acids, Mater. Sci. Eng. C 105 (2019) 110042.
[21] M.A. Chidiebere, E.E. Oguzie, L. Liu, Y. Li, F. Wang, Ascorbic acid as corrosion inhibitor for Q235 mild steel in acidic environments, J. Ind. Eng. Chem. 26 (2015) 182–192.
[22] L. Mydlova, K. Kluza, M. Halama, M. Makowska-Janusik, Anti-corrosive surface effect of ascorbic acid caused on the ZnO nanoparticles—Experimental and theoretical investigations, Appl. Surf. Sci. 483 (2019) 562–571.
[23] ASTM D 3359–92a, Standard Test Methods for Measuring Adhesion by Tape Test, ASTM (1992).
[24] Y.X. Yang, Z. Fang, Y.H. Liu, Y.C. Hou, L.G. Wang, Y.F. Zhou, S.J. Zhu, R.C. Zeng, Y.F. Zheng, S.K. Guan, Biodegradation, hemocompatibility and covalent bonding mechanism of electrografting polyethylacrylate coating on Mg alloy for cardiovascular stent, J. Mater. Sci. Technol. 46 (2020) 114–126.
[25] A. Scurria, C. Scolaro, S. Sfameni, G. Di Carlo, M. Pagliaro, A. Visco, R. Ciriminna, Towards AquaSun practical utilization: Strong adhesion and lack of ecotoxicity of solar-driven antifouling sol-gel coating, Prog. Org. Coat. 165 (2022) 106771.
[26] J. Sun, S. Cai, J. Sun, K. Shen, J. Liu, G. Xu, Ultrasonic aqueous synthesis of corrosion resistant hydroxyapatite coating on magnesium alloys for the application of long-term implant, Ultrason. Sonochem. 58 (2019) 104677.
[27] X.L. Fan, Y.F. Huo, C.Y. Li, M.B. Kannan, X.B. Chen, S.K. Guan, R.C. Zeng, Q.L. Ma, Corrosion resistance of nanostructured magnesium hydroxide coating on magnesium alloy AZ31: influence of EDTA, Rare Met. 38 (2019) 520–531.
[28] Y. Guo, Y. Su, R. Gu, Z. Zhang, G. Li, J. Lian, L. Ren, Enhanced corrosion resistance and biocompatibility of biodegradable magnesium alloy modified by calcium phosphate/collagen coating, Surf. Coat. Technol. 401 (2020) 126318.
[29] X. Mo, J. Qian, Y. Chen, W. Zhang, P. Xian, S. Tang, C. Zhou, N. Huang, H. Ji, E. Luo, H. Zhang, G. Wan, Corrosion and degradation decelerating alendronate embedded zinc phosphate hybrid coating on biodegradable Zn biomaterials, Corros. Sci. 184 (2021) 109398.
[30] L. Fathyunes, V. khalili, Effect of ultrasonic waves on the electrochemical deposition of calcium phosphate/nano-sized silica composite coating, J. Mater. Res. Technol. 14 (2021) 2345–2356.
[31] P. Makkar, H.J. Kang, A.R. Padalhin, O. Faruq, B. Lee, In-vitro and in-vivo evaluation of strontium doped calcium phosphate coatings on biodegradable magnesium alloy for bone applications, Appl. Surf. Sci. 510 (2020) 145333.
[32] J.G. Acheson, L. Robinson, S. McKillop, S. Wilson, M.J. McIvor, B.J. Meenan, A.R. Boyd, TOFSIMS and XPS characterisation of strontium in amorphous calcium phosphate sputter deposited coatings, Mater. Charact. 171 (2021) 110739.
[33] H. Zhou, J. Li, J. Li, Q. Ruan, W. Jin, Z. Yu, W. Li, P.K. Chu, Calcium phosphate coating on biomedical WE43 magnesium alloy pretreated with a magnesium phosphate layer for corrosion protection, Surf. Coat. Technol. 401 (2020) 126248.
[34] G.Y. Liu, J. Hu, Z.K. Ding, C. Wang, Formation mechanism of calcium phosphate coating on micro-arc oxidized magnesium, Mater. Chem. Phys. 130 (2011) 1118–1124.
[35] X.B. Chen, N. Birbilis, T.B. Abbott, A simple route towards a hydroxyapatite-$Mg(OH)_2$ conversion coating for magnesium, Corros. Sci. 53 (2011) 2263–2268.
[36] T. Ishizaki, N. Kamiyama, E. Yamamoto, S. Kumagai, T. Sudare, N. Saito, Communication—In Situ Formation of Anticorrosive $Mg(OH)_2$/Carbon Composite Film on Magnesium Alloy by Ascorbic Acid-Assisted Hydrothermal Process, J. Electrochem. Soc. 162 (2015) C741–C743.
[37] H. Liu, B. Fan, G. Fan, X. Zhao, Z. Liu, H. Hao, B. Yang, Long-term protective mechanism of poly(N-methylaniline)/phosphate one-step electropolymerized coatings for copper in 3.5% NaCl solution, J. Alloy. Compd. 872 (2021) 159752.
[38] C.Y. Li, L. Gao, X.L. Fan, R.C. Zeng, D.C. Chen, K.Q. Zhi, In vitro degradation and cytocompatibility of a low temperature in-situ grown self-healing Mg-Al LDH coating on MAO-coated magnesium alloy AZ31, Bioact. Mater. 5 (2020) 364–376.
[39] M. Toorani, M. Aliofkhazraei, M. Mahdavian, R. Naderi, Superior corrosion protection and adhesion strength of epoxy coating applied on AZ31 magnesium alloy pre-treated by PEO/Silane with inorganic and organic corrosion inhibitors, Corros. Sci. 178 (2021) 109065.
[40] Y. Tang, L. Zhu, P. Zhang, K. Zhao, Z. Wu, Enhanced corrosion resistance of bio-piezoelectric composite coatings on medical magnesium alloys, Corros. Sci. 176 (2020) 108939.
[41] P. Liu, J.M. Wang, X.T. Yu, X.B. Chen, S.Q. Li, D.C. Chen, S.K. Guan, R.C. Zeng, L.Y. Cui, Corrosion resistance of bioinspired DNA-induced Ca–P coating on biodegradable magnesium alloy, J. Magnes. Alloy. 7 (2019) 144–154.
[42] W. Huang, B. Xu, W. Yang, K. Zhang, Y. Chen, X. Yin, Y. Liu, Z. Ni, F. Pei, Corrosion behavior and biocompatibility of hydroxyapatite/magnesium phosphate/zinc phosphate composite coating deposited on AZ31 alloy, Surf. Coat. Technol. 326 (2017) 270–280.
[43] Y.B. Zhao, L.Q. Shi, L.Y. Cui, C.L. Zhang, S.Q. Li, R.C. Zeng, F. Zhang, Z.L. Wang, Corrosion resistance of silane-modified hydroxyapatite films on degradable magnesium alloys, Acta Metall. Sin. Engl. Lett. 31 (2017) 180–188.
[44] S. Wen, X. Liu, J. Ding, Y. Liu, Z. Lan, Z. Zhang, G. Chen, Hydrothermal synthesis of hydroxyapatite coating on the surface of medical magnesium alloy and its corrosion resistance, Prog. Nat. Sci. Mater. Int. 31 (2021) 324–333.
[45] R.C. Zeng, Y. Hu, S.K. Guan, H.Z. Cui, E.H. Han, Corrosion of magnesium alloy AZ31: The influence of bicarbonate, sulphate, hydrogen phosphate and dihydrogen phosphate ions in saline solution, Corros. Sci. 86 (2014) 171–182.
[46] D. Liu, K. Savino, M.Z. Yates, Coating of hydroxyapatite films on metal substrates by seeded hydrothermal deposition, Surf. Coat. Technol. 205 (2011) 3975–3986.
[47] X.B. Chen, N. Birbilis, T.B. Abbott, Effect of [Ca^{2+}] and [PO_4^{3-}] levels on the formation of calcium phosphate conversion coatings on die-cast magnesium alloy AZ91D, Corros. Sci. 55 (2012) 226–232.
[48] J. Wang, F. Witte, T. Xi, Y. Zheng, K. Yang, Y. Yang, D. Zhao, J. Meng, Y. Li, W. Li, K. Chan, L. Qin, Recommendation for modifying current cytotoxicity testing standards for biodegradable magnesium-based materials, Acta Biomater 21 (2015) 237–249.
[49] Z. Cui, Y. Zhang, Y. Cheng, D. Gong, W. Wang, Microstructure, mechanical, corrosion properties and cytotoxicity of betacalcium polyphosphate reinforced ZK61 magnesium alloy composite by spark plasma sintering, Mater. Sci. Eng. C 99 (2019) 1035–1047.
[50] L.Y. Li, L.Y. Cui, B. Liu, R.C. Zeng, X.B. Chen, S.Q. Li, Z.L. Wang, E.H. Han, Corrosion resistance of glucose-induced hydrothermal calcium phosphate coating on pure magnesium, Appl. Surf. Sci. 465 (2019) 1066–1077.
[51] X.M. Wang, X.T. Yu, Y.Z. Hong, R.C. Zeng, Comparison of corrosion resistance of phenylalanine, methionine, and asparagine-induced Ca-P coatings on AZ31 magnesium alloys, Acta Metall. Sin. 10 (2021) 1259–1271.
[52] X.L. Fan, C.Y. Li, Y.B. Wang, Y.F. Huo, S.Q. Li, R.C. Zeng, Corrosion resistance of an amino acid-bioinspired calcium phosphate coating on magnesium alloy AZ31, J. Mater. Sci. Technol. 49 (2020) 224–235.
[53] M.-S. Hong, S.-H. Kim, S.-Y. Im, J.-G. Kim, Effect of ascorbic acid on the pitting resistance of 316L stainless steel in synthetic tap water, Met. Mater. Int. 22 (2016) 621–629.
[54] I. Sekine, Y. Nakahata, H. Tanabe, The corrosion inhibition of mild steel by ascorbic and folic acids, Corros. Sci. 28 (1988) 987–1001.
[55] A.P. Loperena, I.L. Lehr, S.B. Saidman, Formation of a cerium conversion coating on magnesium alloy using ascorbic acid as additive. Characterisation and anticorrosive properties of the formed films, J. Magnes. Alloy. 4 (2016) 278–285.